Carbon Trends 19 (2025) 100491

Contents lists available at ScienceDirect

Carbon Trends

journal homepage: www.elsevier.com/locate/cartre

Graphene-modified g-C_3N_4/ α-Fe_2O_3 systems for light-induced hydrogen generation

Wassila Touati [a,1,*], Miroslava Filip Edelmannová [g,1], Mohamed Karmaoui [a,e], Ahmed Bekka [a], Clarisse Furgeaud [b,c], Chakib Alaoui [a], Imene kadi Allah [a], Bruno Figueiredo [d], J.A. Labrincha [e], Raul Arenal [b,c,f], Kamila Koci [g,*], David Maria Tobaldi [h]

[a] Laboratoire de Chimie des Matériaux Inorganiques Et Applications, Faculté de Chimie, Université des Sciences Et de la Technologie d'Oran, El-Mnaouer, Algeria
[b] Instituto de Nanociencia y Materiales de Aragon (INMA), CSIC-Universidad de Zaragoza, 50009 Zaragoza, Spain
[c] Laboratorio de microscopias avanzadas (LMA), U. Zaragoza, C/ Mariano Esquillor s/n, 50018 Zaragoza, Spain
[d] Graphenest, Lugar da Estação, Edifício Vouga Park, 3740-070, Paradela do Vouga, Portugal
[e] Department of Materials and Ceramic Engineering/CICECO–Aveiro Institute of Materials, University of Aveiro, Campus Universitário de Santiago, 3810-193 Aveiro, Portugal
[f] ARAID Foundation, 50018 Zaragoza, Spain
[g] Institute of Environmental Technology, CEET,VŠB-Technical University of Ostrava, 17.listopadu 15/2172, Ostrava-Poruba, 70800, Czech Republic
[h] CNR NANOTEC Institute of Nanotechnology, Via Monteroni, Lecce 73100, Italy

ARTICLE INFO

Keywords:
Water splitting
g-C_3N_4/ α-Fe_2O_3
g-C_3N_4/ α-Fe_2O_3/graphene
Photocatalysis

ABSTRACT

Photocatalysis represents an advanced and efficient technology for harnessing light energy. The non-toxicity, affordability, and versatility of this technique render it particularly attractive for hydrogen production via water splitting. Nevertheless, the primary challenge lies in identifying materials capable of efficiently catalyzing the water splitting reaction upon exposure to light. This study presents the influence of the quantity of hematite and graphene on g-C_3N_4 in the context of hydrogen generation from methanol-water decomposition under UVC irradiation. Pure g-C_3N_4 exhibits the highest hydrogen generation efficiency. However, adding hematite decreases photocatalytic efficiency, likely due to the formation of a type II heterojunction between α-Fe_2O_3 and g-C_3N_4, which reduces the overall reduction capacity of the system. While incorporating graphene into the g-C_3N_4/ α-Fe_2O_3 system enhances photocatalytic efficiency by improving electron mobility and prolonging the lifetime of photo-generated excitons, the highest yield was achieved with BUF10/GNP0.5. This research offers valuable insights into charge transfer and separation processes for photo-generated excitons within the g-C_3N_4/α-Fe_2O_3 and g-C_3N_4/α-Fe_2O_3/graphene systems in the context of light-induced hydrogen production.

1. Introduction

Hydrogen (H_2) has become a major focus of global attention due to its potential for reducing greenhouse gas emissions and boosting the economy. Its high energy density has made it possible to develop decentralised renewable energy sources and green mobility solutions, which could pave the way for the future of energy transition. Photocatalytic water splitting using a semiconductor photocatalyst is a promising method for producing hydrogen, as it enables solar-to-chemical energy conversion and offers a cost-effective alternative to traditional production processes such as electrolysis and oil reforming [1–4]. To date, various photocatalysts have been developed for water splitting reaction, such as TiO_2, CdS, MoS_2, $BiVO_4$ and WO_3 [5–10]. However, these photocatalysts are hindered by their limited light response range, and rapid recombination of photogenerated electron and hole pairs [11–14]. To overcome these issues, the development of efficient photocatalysts for enhancing the water splitting reaction is of the highest priority. Graphitic carbon nitride (g-C_3N_4), is a two-dimensional (2D), polymeric material, in which carbon and nitrogen atoms are arranged in a hexagonal structure, in a fashion similar to

* Corresponding authors.
E-mail addresses: wassila.touati@univ-usto.dz (W. Touati), Kamila.Koci@vsb.cz (K. Koci).
[1] These authors equally contributed to the paper.

https://doi.org/10.1016/j.cartre.2025.100491
Received 15 March 2024; Received in revised form 21 January 2025; Accepted 24 February 2025
Available online 26 February 2025
2667-0569/© 2025 The Authors. Published by Elsevier Ltd. This is an open access article under the CC BY-NC-ND license (http://creativecommons.org/licenses/by-nc-nd/4.0/).

graphite, and connected by covalent bonds to form a continuous network, has attracted considerable interest [15–21]. The 2D g-C_3N_4 sheets are linked each-other by covalent bonds, and stacked with the aid of van der Waals interactions between the layers, resulting in good thermal and chemical stability [19]. Importantly, g-C_3N_4 is visible light responsive, being its band gap of ~2.7 eV (459 nm), and permits water/proton reduction with a significant driving force, due to its negative conduction band (CB) potential [22,23]. As a result, this polymeric photocatalyst become extremely attractive in pollutant degradation, water splitting and CO_2 reduction reactions [24–28]. However, the fast recombination of photogenerated electron and hole pairs result in low efficiency in photocatalytic performance, which restricts its practical use [29,30]. Therefore, constructing heterostructures by coupling g-C_3N_4 with another semiconductor having a suitable band structure is considered as a promising strategy for increasing the lifetime of photogenerated charge carriers, improving the charge carrier separation efficiency, and even enhancing light utilisation, therefore enhancing the photocatalytic performance [31–35]. Hematite (α-Fe_2O_3), an earth-abundant and environmentally benign iron oxides, is widely employed as a photocatalyst for pollutant removal due to its significant photo-oxidation power [36]. It has attracted significant interest for combination with g-C_3N_4 due to its narrow bandgap of approximately 2.1 eV (590 nm) and favourable band edge positions [37]. Besides, graphene has gained considerable interest because of its thermal, optical and electrical properties [38], as well as its numerous applications in the field of photocatalysis. A recent study revealed that a synergistic effect between Fe(III) species and graphene results in stronger light absorption, and lower charge recombination [39]. However, difficulties in precise structural control between multiple components, and the nanostructural control of each component limit the activity of the photocatalysis, which plays a key role in the photocatalytic efficiency in a multicomponent system [40]. Literature reports that the g-C_3N_4/α-Fe_2O_3/graphene system increased the photocatalytic performance of g-C_3N_4 in various applications [41–43]. Nevertheless, limited reports exist on the synthesis and application of the g-C_3N_4/α-Fe_2O_3/graphene system in hydrogen production from water splitting, employing a straightforward preparation method.

In this study, the surface of bulk g-C_3N_4 was modified with graphene and α-Fe_2O_3 by a facile synthesis followed by ultrasonication. The as-prepared materials were investigated in the photocatalytic hydrogen production from the methanol–water mixture. Thus, the effect of the amount of graphene and α-Fe_2O_3 on the yield of photocatalytic hydrogen generation is discussed. This study contributes to understanding the charge transfer and separation processes within the constructed heterojunctions, offering a rational design strategy for g-C_3N_4/α-Fe_2O_3 and g-C_3N_4/α-Fe_2O_3/graphene photocatalysts applied in H_2 production and environmental remediation under UVC irradiation. Those results might be of use in data-driven catalysis research.

2. Materials and methods

2.1. Materials

Urea (CH_4N_2O, 99 %), hexanol ($CH_3(CH_2)_5OH$) and iron nitrate ($Fe(NO_3)_3{\cdot}9H_2O$) were obtained by Sigma-Aldrich, graphene nanoplatelets (GNPs), dispersed in ethanol, were supplied by Graphenest. All reactants were used as received, without further purification

2.2. Sample preparation

Bulk g-C_3N_4 powder was prepared via the thermal polymerisation of urea [44]. In a typical process, 10 g of urea was placed in a covered crucible and heated in air at 550 °C for 4 h at a ramp rate of 10 °C min^{-1}. The resulting yellow product was collected and ground into a powder.

Hematite (α-Fe_2O_3) was synthesised using a low temperature non-aqueous sol-gel route. 1 mmol of $Fe(NO_3)_3{\cdot}9H_2O$ (0.808 g) was dissolved in 15 mL of anhydrous hexanol. After 30 min of stirring (solution clear and dissolved), the mixture was transferred into an autoclave and heated at 180 °C for 36 h. The resulting precipitates were washed with ethanol several times, and dried in air at 60 °C [45].

To obtain 0.5 g of the binary g-C_3N_4-α-Fe_2O_3 heterojunction with (5 wt% and 10 wt%) of α-Fe_2O_3, a suitable amount of bulk g-C_3N_4 and α-Fe_2O_3 were mixed, and 15 mL of ethanol were added to the mixture. After sonication for 1 h, the mixture was dried in air at 60 °C. The same procedure was followed to obtain the ternary g-C_3N_4-α-Fe_2O_3-GNPs heterojunction with (5 wt% and 10 wt%) of α-Fe_2O_3 and (0.5 wt% and 1 wt%) of GNPs. The schematic representation of sample preparation is shown in Figure S1.

The prepared materials are referred as indicated in Table 1.

2.3. Sample characterisation

X-ray powder diffraction (XRPD) was performed to identify the mineralogy of the samples. Patterns were carried out at room temperature on a diffractometer (PANalytical X'Pert Pro, NL), equipped with a fast RTMS detector (PIXcel 1D, PANalytical), with Cu Ka radiation (45 kV and 40 mA, 20–80 °2θ range, with a virtual step scan of 0.02 °2θ, and virtual time per step of 200 s). Morphology was revealed by high-resolution transmission electron microscopy (HRTEM) imaging using an FEI Titan 60–300 kV transmission electron microscope (TEM) equipped with a spherical aberration corrector (CETCOR Cs-objective CEOS Company) and working at 80 kV. All the specimens were dispersed in isopropanol using an ultrasonic bath and dropped into a copper grid coated with a holey carbon film. Optical spectra of the prepared samples were recorded on a Shimadzu UV-3100 spectrometer (JP), equipped with an integrating sphere, and a white reference material made of Spectralon. Diffuse reflectance spectra (DRS) were obtained in the UV–Vis spectral range (250–750 nm), using 0.2 nm resolution. The measured reflectance spectra were converted into pseudo-absorption spectra according to the Kubelka-Munk transformation [46]. The optical band gap (E_g) of the materials was calculated by means of the differential approach [47], and from the converted DR spectra, using the Tauc procedure following direct and indirect transitions [48], as described in a previous report [49].

2.4. Functional properties: Hydrogen generation tests

The photocatalytic experiments were conducted in a stirred batch photoreactor made of stainless steel (with a volume of 348 mL). The reaction mixture consisted of 50 % methanol in distilled water, along with 0.1 g of photocatalyst. Prior to the reaction, the mixture was purged with helium to remove air. An 8 W Hg lamp with a peak intensity at 254 nm wavelength (Ultra-Violet Products Inc.) was positioned on a quartz glass window on the top of the photoreactor as the radiation source. After sealing the photoreactor (with the UVC lamp on), a gas sample was taken via a septum using a syringe at the start of the reaction (at time 0 h). The gas samples were analysed using a Shimadzu Tracera GC-

Table 1
Designation of the prepared samples.

Designation	Description
BU	Bulk g-C_3N_4 made with urea
BUF5	Modified bulk g-C_3N_4 made with urea and 5 wt.% α-Fe_2O_3
BUF10	Modified bulk g-C_3N_4 made with urea and 10 wt.% α-Fe_2O_3
BUF5/GNP0.5	Modified bulk g-C_3N_4 made with urea and 5 wt.% α-Fe_2O_3/ 0.5 wt.% GNPs
BUF5/GNP1	Modified bulk g-C_3N_4 made with urea and 5 wt.% α-Fe_2O_3/ 1 wt.% GNPs
BUF10/GNP0.5	Modified bulk g-C_3N_4 made with urea and 10 wt.% α-Fe_2O_3/ 0.5 wt.% GNPs
BUF10/GNP1	Modified bulk g-C_3N_4 made with urea and 10 wt.% α-Fe_2O_3/ 1 wt.% GNPs

2010Plus gas chromatograph equipped with a barrier discharge ionization detector (GC/BID). The reaction mixture underwent irradiation, and gas samples were collected after 1, 2, 3, and 4 h for further analysis. The provided results represent the average of three tests, ensuring a high degree of reproducibility across all measurements. This underscores the reliability of the observed activity in the samples.

3. Results and discussion

3.1. XRPD and morphological analysis

The XRPD patterns of the as-prepared samples are displayed in Fig. 1a-b. Those of pure g-C_3N_4, pure α-Fe_2O_3 and g-C_3N_4- α-Fe_2O_3 heterojunction (BU, α-Fe_2O_3, BUF5, BUF10, respectively) are shown in Fig. 1a. The two distinct characteristic peaks of pure hexagonal g-C_3N_4 are well featured according to JCPDS N°87–1526. The weak peak at around 2Θ = 13°, that corresponds to the reflection (100) is related to the repeated tri-s-thiazine units, the stronger peak at around 2Θ = 27.5° which corresponds to the basal reflection (002) is attributed to the interlayer graphitic like structure [50,51]. Hematite confirms to crystallise in the standard hexagonal phase as reported in JCPDS N°33–0664 [52]. The presence of strong and sharp diffraction peaks indicates that the sample is highly crystalline. Reflections of both bulk g-C_3N_4 and α-Fe_2O_3 can be found in the modified binary compound (BUF5 and BUF10, respectively), which is an indication of its successful synthesis.

Fig. 1b displays XRPD patterns of bulk g-C_3N_4 modified with both hematite and graphene (*i.e.*, specimens: BUF5/GNP0.5, BUF5/GNP1, BUF10/GNP0.5, BUF10/GNP1, respectively). All peaks in the diffraction patterns are successfully indexed for the ternary compound, except for the one corresponding to graphene This discrepancy may be attributed to the small quantity of graphene utilised in the composite, and similar outcomes are documented in the literature [39]. Fig. 2a-d show TEM and high magnification TEM (HRTEM) images of BU and BUF10/GNP1. In Fig. 2a g-C_3N_4 (BU) exhibits a sheet-like morphology, the grey contrast is related to different sheet thicknesses. Fig. 2c presents TEM images of modified g-C_3N_4 with hematite (10 W*t*%) and graphene 1 % named (BUF10-GNP1). It is evident that α-Fe_2O_3 NPs were uniformly distributed on the surface of g-C_3N_4, confirming the successful synthesis of our compound. However, the presence of graphene is not clearly visible in the images. The challenge arises from the fact that both g-C_3N_4 and graphene are nanosheets, making their distinction challenging [53]. Fig. 2b,d correspond to high magnification TEM micrographs taken in the same area. Although fast Fourier transform (FFT) patterns (insets in Fig. 2b,d) indicate local structural order in pure and modified g-C_3N_4 specimens, their overall appearance is mostly amorphous, as shown by the contrast in Fig. 2b,d. The EDX and electron energy loss spectra (EELS) data analyses are depicted in Figure S2 and S3. In Figure S2a, it is discerned that bulk g-C_3N_4 exhibits, in addition to carbon and nitrogen, trace amounts of silicon, attributed to likely impurities in the raw material. The EEL spectrum, Figure S2b, manifests pronounced C K-edge and N K-edge peaks, indicative of the presence of sp^2-hybridised carbon and nitrogen atoms [54]. This observation is further confirmed by the visible 1 s→π* transition for both elements [55]. The calculated C/N ratio from EELS, found to be 0.69, closely aligns with the reported value for bulk g-C_3N_4 in the literature (0.71) [56]. Similar analytical considerations apply to sample BUF10/GNP1, as illustrated in Figure S3, with the additional presence of iron and oxygen assigned to the Fe_2O_3 nanocrystals in the system. It must be noted that it was not possible to acquire EELS spectra on the Fe_2O_3 nanocrystals because of their excessive thickness.

3.2. Optical properties

UV–vis diffuse reflectance spectroscopy (Fig. 3a-d) was employed to examine the optical absorption properties of the prepared specimens, a critical factor influencing photocatalytic activity. As illustrated in Fig. 3a,b, pure g-C_3N_4 and hematite exhibit absorption edges at around 459 nm, and 589 nm, respectively. In the hematite spectrum (Fig. 3b), absorptions near 430 nm, corresponding to the $^6A_1 \rightarrow {}^4E$ ligand field transitions of Fe^{3+}, and the feature at around 550–600 nm, assigned to the $^6A_1 + {}^6A_1 \rightarrow {}^4T_1({}^4G) + {}^4T_1({}^4G)$ excitation of an Fe−Fe pair, are noticeable [57].

A decrease in reflectance can be noticed in the modified binary and ternary specimens, with α-Fe_2O_3 and α-Fe_2O_3/graphene (Fig. 3c-d). This is due to the change in colour from yellowish (pure g-C_3N_4) to a darker hue, resulting from the addition of graphene and hematite to the system [58]. In addition, the spectra exhibit the two distinct absorbance stages, corresponding to the optical absorbance of g-C_3N_4 and hematite [59].

The E_g of the samples were estimated from DR spectra using the Tauc plot, considering both indirect and direct interband transitions [60–62], and the differential reflectance method [63]; they are listed in Table 2. The reported E_g of pure g-C_3N_4 and pure α-Fe_2O_3 are ~2.7 eV (459 nm) and ~2.1 eV (589 nm) respectively [64,65], which are in accordance with the calculated indirect interband transition for g-C_3N_4, and direct interband transition for α-Fe_2O_3. Therefore, in this study, an indirect transition seems to be more appropriate for pure g-C_3N_4, whilst a direct

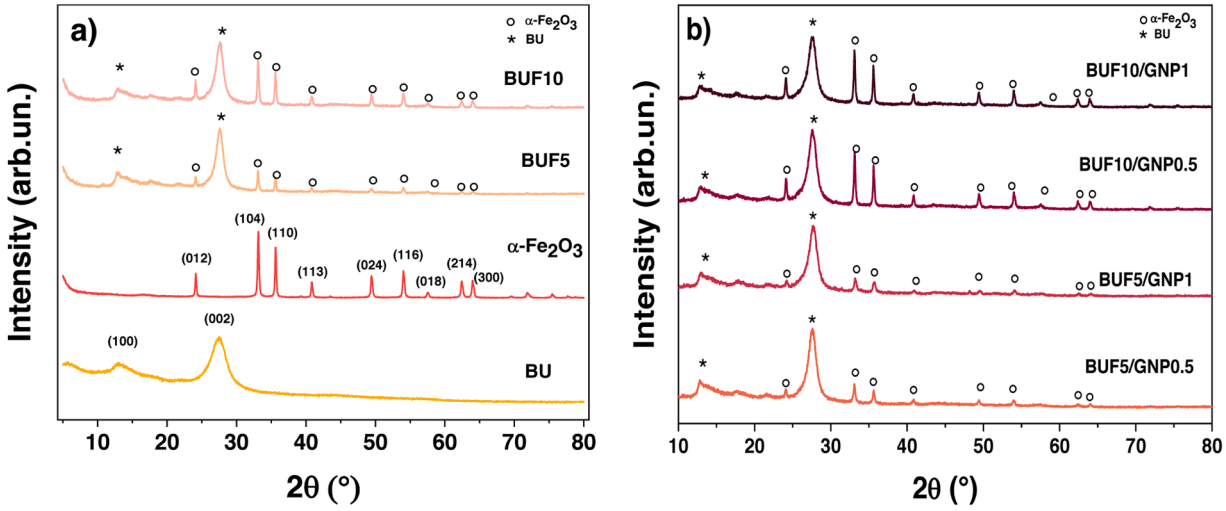

Fig. 1. a) XRPD patterns of bulk g-C_3N_4, hematite (α-Fe_2O_3), modified bulk g-C_3N_4 with hematite (5 and 10 w*t*%), named: BU, α-Fe_2O_3, BUF5, BUF10, respectively. b) XRPD patterns of modified bulk g-C_3N_4 with hematite and graphene 5 w*t*% of hematite with (0.5 and 1 w*t*%) of graphene and 10 w*t*% of hematite with (0.5 and 1 w*t*%) of graphene, named BUF5/GNP0.5, BUF5/GNP1, BUF10/GNP0.5, BUF10/GNP1, respectively.

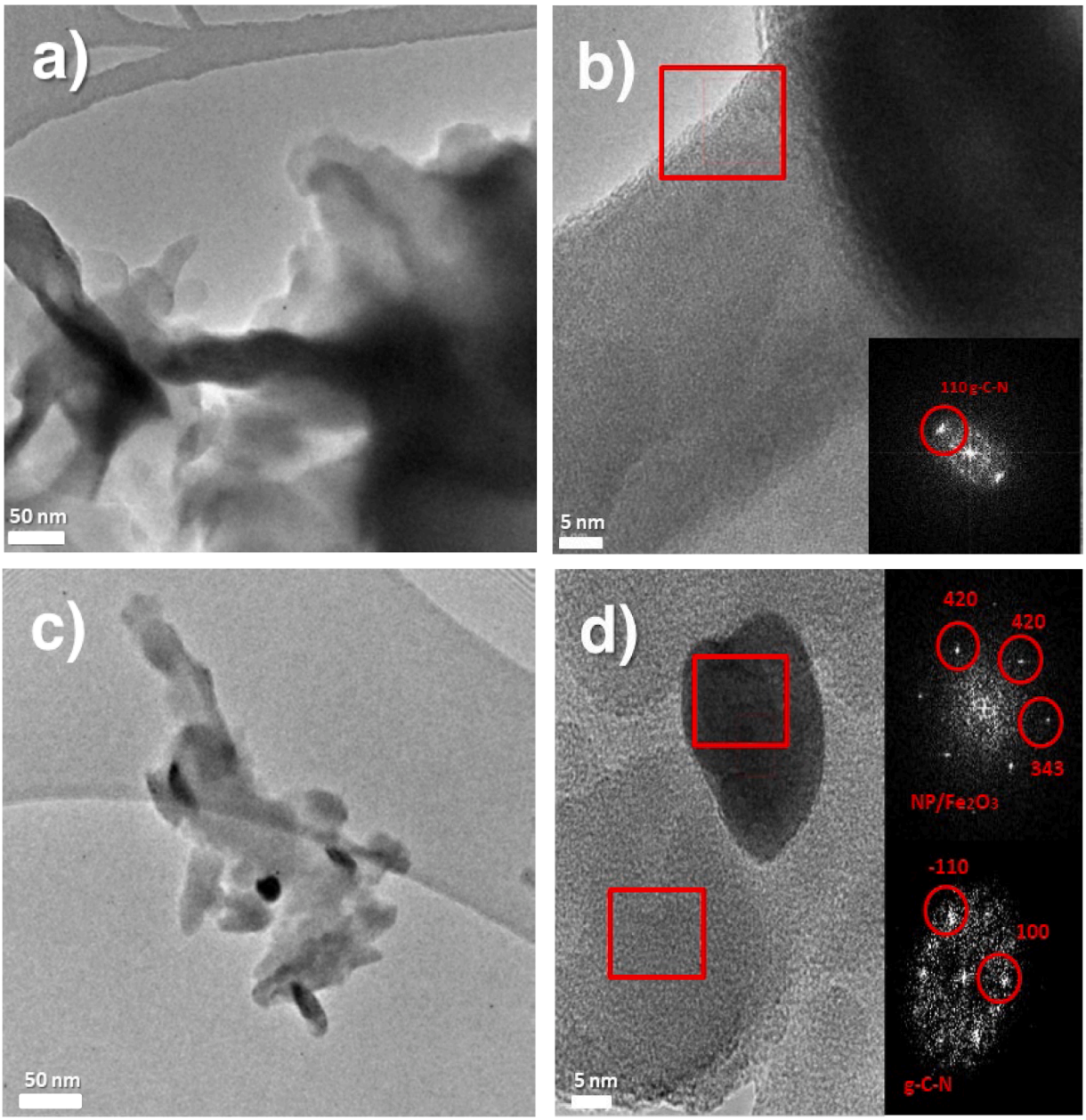

Fig. 2. Low-magnification TEM and HRTEM images of (a-b) bulk g-C_3N_4 (c -d). Modified g-C_3N_4 with hematite and graphene (10 wt% of hematite with 1 wt% of graphene), BUF10/GNP1.

transition suits well for pure α-Fe_2O_3. However, it has to be stressed that one of the limitations of the absorption function method is that it consider the analysed specimen to be composed of one single E_g, which is different from the modified g-C_3N_4 (binary and ternary compound with α-Fe_2O_3 and α-Fe_2O_3/graphene), hence, in this particular case, it is preferable to use the differential reflectance method to estimate the E_g [66].

4. Photocatalytic induced H_2-production

The results of photocatalytic hydrogen production are illustrated in Fig. 4a-b, demonstrating the dependence of H_2 yields from the decomposition of a methanol-water mixture during 4 h of irradiation time. A notable influence of hematite content on the photocatalytic activity of g-C_3N_4 is observed. The highest amount of H_2 is generated with unmodified g-C_3N_4. The photocatalysts follow this order: BU > BUF10/GNP0.5 > BUF10/GNP1 > BUF5/GNP0.5 > BUF5/GNP1 > BUF10 > BUF5. In comparison to the g-C_3N_4/α-Fe_2O_3 binary compounds, ternary α-Fe_2O_3/graphene-modified compounds exhibit enhanced photocatalytic performance. The impact of hematite and graphene amounts on g-C_3N_4 photocatalytic hydrogen generation is depicted in Fig. 5 (a-b) for all of the investigated photocatalysts. Moreover, the materials exhibit high photocatalytic performance in comparison to other 2D g-C_3N_4-based heterostructure photocatalysts reported in the literature, as shown in Table S1. However, it is important to note that a direct like-with-like comparison may pose challenges due, for instance, to variations in the total irradiated area of the reactor, radiant flux reaching the reactor, and the total volume of the reactor among different studies. To address this, the data are not only reported in terms of H_2 generation rate, but also as apparent quantum efficiency.

To elucidate the reaction mechanisms of the photocatalysts, the positions of the conduction and valence bands play a crucial role. These values enable the construction of a schematic diagram depicting the photo-generated electron-hole separation process. At this aim, at the

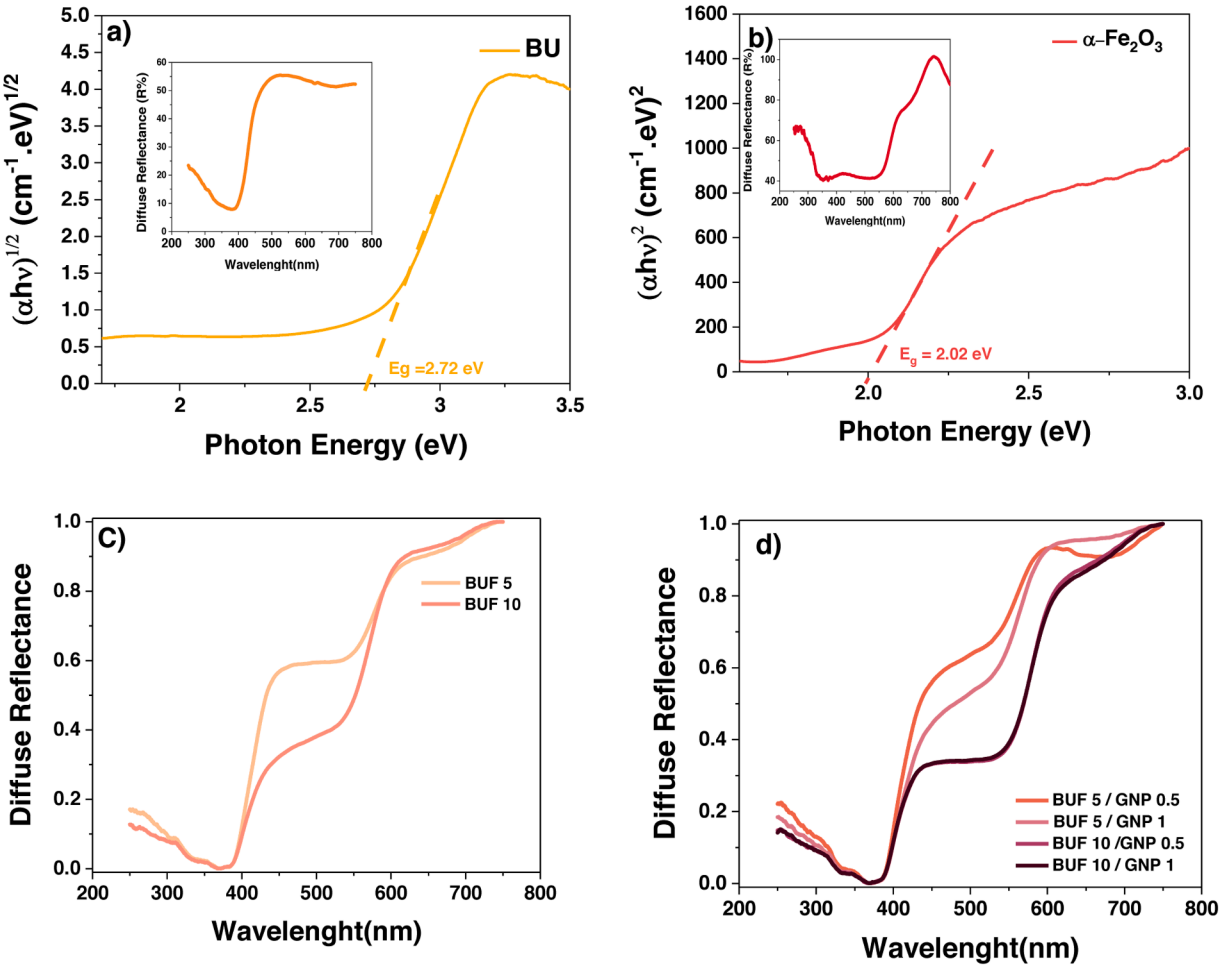

Fig. 3. UV–VIS diffuse reflectance spectra of a) bulk g-C_3N_4 b) α-Fe_2O_3 c) modified bulk g-C_3N_4 with hematite (5 and 10 wt%) d) modified bulk g-C_3N_4 with hematite and graphene 5 wt% of hematite with (0.5 and 1 wt%) of graphene and 10 wt% of hematite with (0.5 and 1 wt%) of graphene, and Tauc plots of a) bulk g-C_3N_4 and b) α-Fe_2O_3.

Table 2
Apparent optical E_g, estimated using the Tauc plot procedure for direct and indirect transitions, and the differential reflectance method (dR/dλ).

Sample	Apparent optical E_g							
	Tauc Plot				dR/dλ			
	Indirect		Direct					
	eV	nm	eV	nm	eV		nm	
BU	2.74	453	3.00	413	2.89		429	
α-Fe_2O_3	1.61	770	2.02	614	2.10		589	
					g-C_3N_4	α-Fe_2O_3	g-C_3N_4	α-Fe_2O_3
BUF5	2.70	459	3.06	405	3.00	2.14	413	579
BUF10	2.53	490	3.02	410	3.04	2.17	407	571
BUF5/GNP0.5	2.79	444	3.08	402	3.04	2.21	407	561
BUF5/GNP1	2.77	447	3.07	403	3.00	2.20	413	563
BUF10/GNP0.5	2.79	444	3.06	405	3.05	2.14	406	579
BUF10/GNP1	2.80	442	3.07	403	3.08	2.14	402	579

point of zero charge, the CB edge (E_{CB}) and the VB edge (E_{VB}) of a semiconductor can be calculated using these equations [67,68]:

$$E_{CB} = c - E^e - 0.5E_g \quad (1)$$

$$E_{VB} = E_{CB} + E_g \quad (2)$$

Where E_{CB} and E_{VB} are the conduction band and valence band edge potential respectively. χ is the absolute electronegativity of a given semiconductor; E^e is the energy of the free electrons (4.5 eV) [69]; E_g is the band gap energy of the semiconductor. The value for the working function (WF) of graphene is (−4.5 eV) [70]. The χ values for g-C_3N_4 and α-Fe_2O_3 are 4.73 and 5.87 eV, respectively [71,72]. E_{NHE} (NHE = normal hydrogen electrode) is related to E_{AVS} (AVS = absolute vacuum scale) as follows [73]:

$$E_{AVS} = E_{NHE} - E^e \quad (3)$$

The positions of the semiconductor's electronic band edge concerning the oxidation/reduction potential levels of water are crucial for

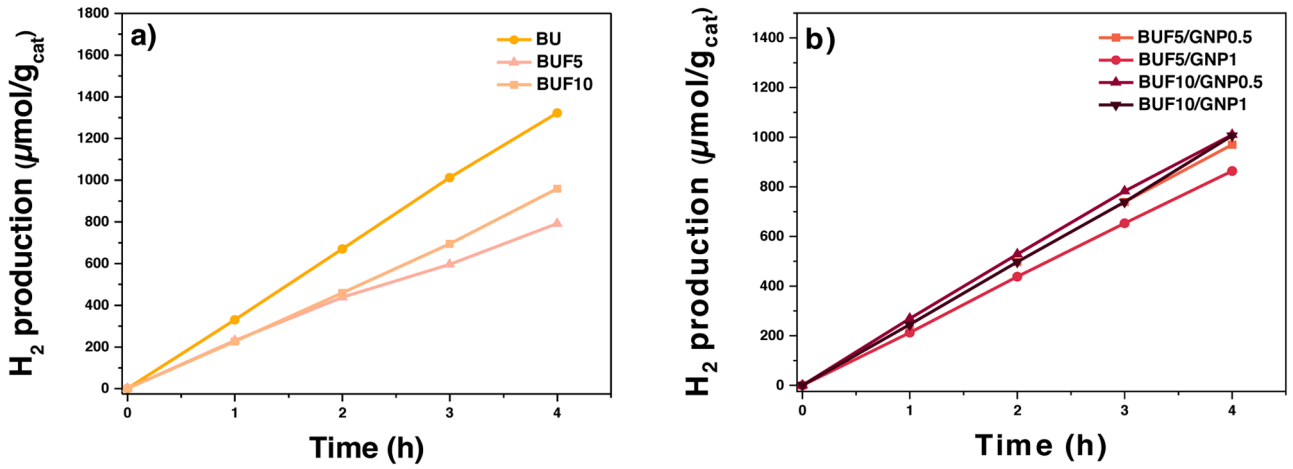

Fig. 4. H_2 production over 4 h of irradiation from the decomposition of a methanol-water mixture, depicted as a function of time for the studied materials.

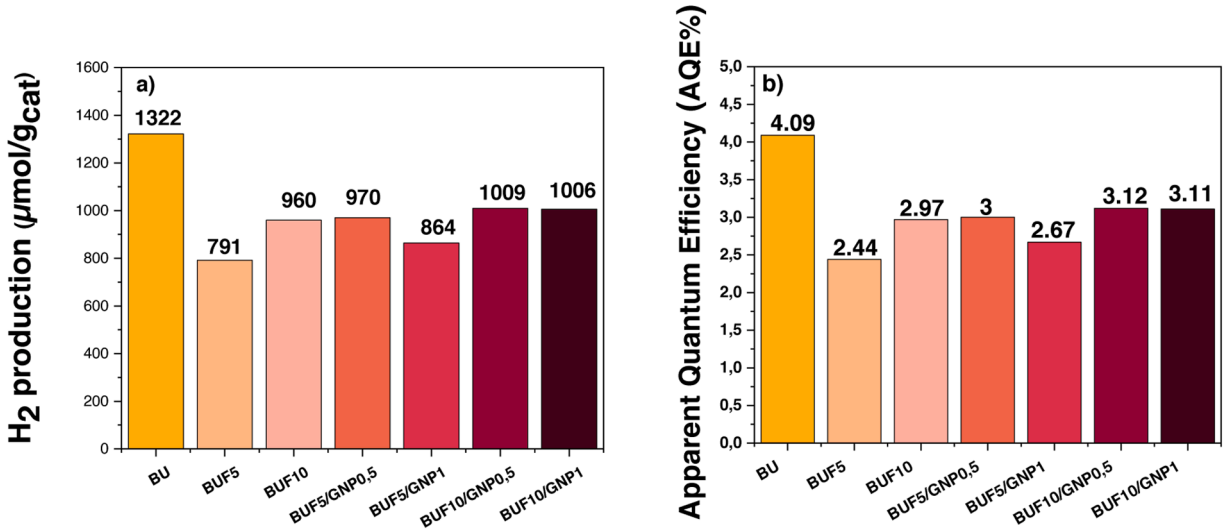

Fig. 5. a) Rate of hydrogen production, b) Apparent quantum efficiency, in the presence of examined photocatalysts after 4 h of illumination.

determining the feasibility of photocatalytic H_2 generation. Therefore, the CB bottom must be more negative than the reduction band bottom (H^+/H_2), while the VB top must be more positive than the oxidation band bottom (H_2O/O_2) (Fig. 6) [74].

In our case, the highest hydrogen yields in modified specimens were observed in BUF10/GNP0.5 and BUF10/GNP1 (after 4 h of irradiation: 1009 μmol/g_{cat}, and 1006 μmol/g_{cat}, respectively). Nevertheless, this yield remains lower than that of pure g-C_3N_4. We have previously demonstrated that the formation of a Schottky barrier at the interface of the binary g-C_3N_4/graphene system does occur. However, it has been observed that the electrons confined within the graphene trap lack the requisite potential to effectively reduce H^+ to hydrogen, resulting in a reduction of hydrogen production [49]. In light of the outcomes obtained from the photocatalytic hydrogen generation experiments involving the binary g-C_3N_4/α-Fe_2O_3 compounds, and considering the relative positions of their conduction bands and the hydrogen redox potential, we propose a mechanism based on a type-II heterojunction, as illustrated in Fig. 7 [49]. This proposed mechanism offers insights into the enhanced efficiency of hydrogen production in the g-C_3N_4/α-Fe_2O_3 system compared to the g-C_3N_4/graphene system, where the Schottky barrier impedes the electron transfer needed for effective reduction of H^+. According to this, excited holes in the VB of α-Fe_2O_3 transfer to the VB of g-C_3N_4, while electrons in the CB of g-C_3N_4 transfer to the CB of α-Fe_2O_3. The photogenerated electrons in the CB of g-C_3N_4 are trapped in the conduction band of α-Fe_2O_3, likely leading to a decrease in reduction capacity. Holes in the VB of α-Fe_2O_3 migrate to the VB of g-C_3N_4, where the oxidation capacity is reduced. Consequently, the g-C_3N_4/ α-Fe_2O_3 system is limited by inefficient interfacial charge transfer processes under UV irradiation. Indeed, exciton trapping, recombination, and interfacial transfer hinder the photocatalytic activity [75]. While our current dataset limits us to speculation, a recently published review paper highlights the low solar-to-hydrogen efficiency of hematite, attributing it to rapid exciton recombination and limited hole mobility [76].

On the other hand, when graphene is included in the system (*i.e.* the graphene/g-C_3N_4/hematite configuration), proves itself advantageous for hydrogen production. Graphene, positioned more favourably for hydrogen generation compared to α-Fe_2O_3, facilitates enhanced electron transfer from g-C_3N_4 to α-Fe_2O_3, as illustrated in Fig. 6. In this study, the introduction of graphene markedly enhances the photocatalytic activity of the g-C_3N_4/α-Fe_2O_3 binary system. However, despite this improvement, the overall activity of both the binary and ternary systems remains lower than that of g-C_3N_4 alone, which exhibits higher activity in photocatalytic H_2 generation. While negative results are often considered as less impactful than positive outcomes in the utilitarian point-of-view of scientific research, such challenges are pervasive in catalysis and materials science. Addressing this issue has become a significant hurdle in data-driven research. Consequently, with the increasing prevalence of

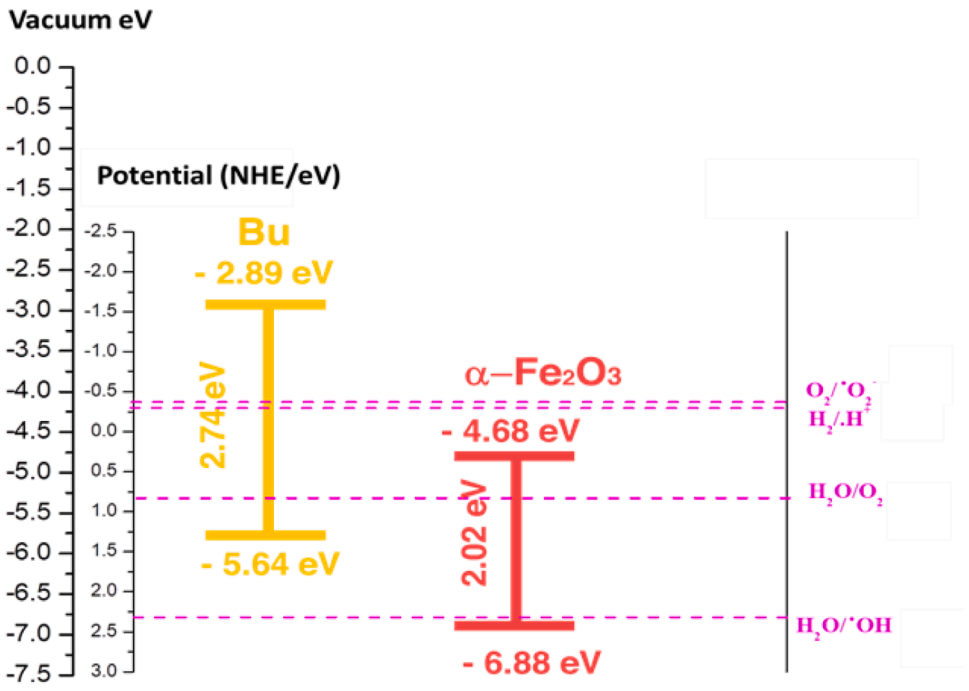

Fig. 6. Band edge positions of g-C_3N_4 and α-Fe_2O_3.

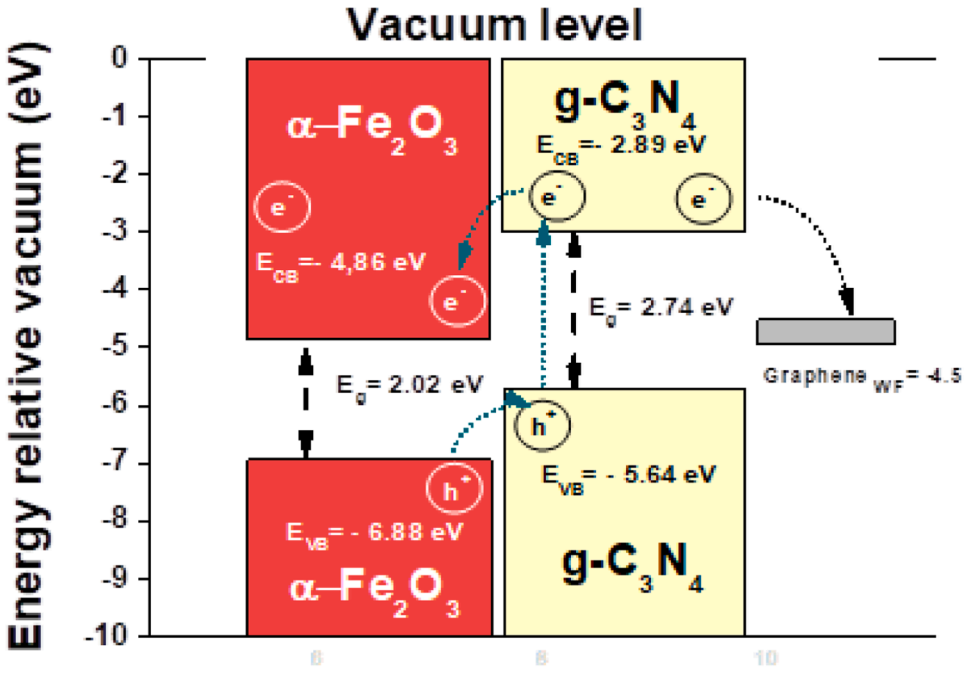

Fig. 7. Proposed mechanism for spatial charge carrier separation in g-C_3N_4 /α-Fe_2O_3/graphene (with UV excitation).

data-driven methodologies, the significance of incorporating negative results for robust machine learning is rapidly gaining recognition [77].

Finally, as commonly recognised, the assessment of photocatalyst reusability is as a pivotal criterion in evaluating photocatalytic materials. Each test conducted for every photocatalyst utilised the same batch, ensuring consistent use of both the photocatalyst and the methanol–water solution throughout the experiments. To ensure reproducibility, each experiment was repeated a minimum of three times. Therefore, as shown in Figure S4, we can confidently assert that the prepared materials demonstrate stability and reusability, at least within the short-term perspective.

5. Conclusion

The impact of α-Fe_2O_3 and graphene content on g-C_3N_4 in photocatalytic H_2 generation under UVC irradiation has been investigated. The highest H_2 generation yield was observed with pure g-C_3N_4, while the addition of hematite decreased the photocatalytic activity's efficiency. This decrease can be attributed to the formation of a type-II heterojunction between α-Fe_2O_3 and g-C_3N_4, where photogenerated electrons from g-C_3N_4 are transferred to the conduction band of α-Fe_2O_3, resulting in a reduction in the system's overall reduction capacity.

However, the introduction of graphene into the binary system (g-

C_3N_4/α-Fe_2O_3) improved H_2 production, with the highest yield achieved in BUF10/GNP0.5. This finding suggests that graphene positively influences the charge transfer and separation mechanisms in the g-C_3N_4/α-Fe_2O_3 and g-C_3N_4/α-Fe_2O_3/graphene heterojunctions. While those data might be perceived as "*negative results*", these insights contribute to a better understanding of the processes underlying hydrogen generation through water splitting, possibly playing a key-role in data driven catalysis approaches.

CRediT authorship contribution statement

Wassila Touati: Writing – review & editing, Writing – original draft, Methodology, Investigation, Formal analysis. **Miroslava Filip Edelmannová:** Writing – review & editing, Writing – original draft, Validation, Investigation, Formal analysis. **Mohamed Karmaoui:** Validation, Methodology. **Ahmed Bekka:** Validation, Methodology. **Clarisse Furgeaud:** Writing – review & editing, Visualization, Validation, Project administration, Funding acquisition. **Chakib Alaoui:** Visualization, Formal analysis. **Imene kadi Allah:** Visualization, Methodology. **Bruno Figueiredo:** Resources. **J.A. Labrincha:** Writing – review & editing, Visualization, Validation, Project administration, Funding acquisition. **Raul Arenal:** Writing – review & editing, Visualization, Validation, Investigation, Funding acquisition. **Kamila Koci:** Writing – review & editing, Writing – original draft, Visualization, Methodology, Investigation, Funding acquisition. **David Maria Tobaldi:** Writing – review & editing, Writing – original draft, Visualization, Validation, Supervision, Methodology, Conceptualization.

Declaration of competing interest

The authors declare that they have no known competing financial interests or personal relationships that could have appeared to influence the work reported in this paper.

Acknowledgments

We would like to express our gratitude to the Algerian Ministry of Higher Education and Scientific Research for funding Wassila Touati's visit to the University of Aveiro, through the National Exceptional Scholarship Program (PNE). R.A. gratefully acknowledges the support from the Spanish MICIU (PID2023-151080NB-I00/AEI/10.13039/501100011033 and CEX2023-001286-S MICIU/AEI /10.13039/501100011033) and by the DGA project E13-23R. The TEM studies were conducted at the Laboratorio de Microscopias Avanzadas, Universidad de Zaragoza, Spain. Kamila Kočí is thankful to the Large Research Infrastructure ENREGAT (project No LM2023056).

This work was partly developed within the scope of the project CICECO-Aveiro Institute of Materials, UIDB/50011/2020, UIDP/50011/2020 & LA/P/0006/2020, financed by national funds through the FCT/MCTES (PIDDAC).

This work was partly supported by the Italian Ministry of Research (MUR) in the framework of the National Recovery and Resilience Plan (NRRP), funded by the European Union – NextGenerationEU, M4C2, within the NRRP project NFFA-DI, CUP B53C22004310006, IR0000015. "I-PHOQS" Grant (CUP B53C22001750006) and under the complementary actions to the NRRP, "Fit4MedRob" Grant (PNC0000007, CUP B53C22006960001) and "ANTHEM" Grant (PNC0000003, CUP B53C22006710001), funded by NextGenerationEU.

Supplementary materials

Supplementary material associated with this article can be found, in the online version, at doi:10.1016/j.cartre.2025.100491.

Data availability

Data will be made available on request.

References

[1] H. Drobná, V. Meinhardová, L. Dubnová, K. Kozumplíková, M. Reli, K. Kočí, L. Čapek, Partially reduced Ni-NiO-TiO2 photocatalysts for hydrogen production from methanol–Water solution, Catalysts. 13 (2023) 293.
[2] Q. Xu, B. Cheng, J. Yu, G. Liu, Making co-condensed amorphous carbon/g-C_3N_4 composites with improved visible-light photocatalytic H_2-production performance using Pt as cocatalyst, Carbon. N. Y. 118 (2017) 241–249.
[3] W. Xing, C. Li, G. Chen, Z. Han, Y. Zhou, Y. Hu, Q. Meng, Incorporating a novel metal-free interlayer into g-C_3N_4 framework for efficiency enhanced photocatalytic H_2 evolution activity, Appl. Catal. B Environ. 203 (2017) 65–71.
[4] X. She, J. Wu, H. Xu, J. Zhong, Y. Wang, Y. Song, K. Nie, Y. Liu, Y. Yang, M.T. F. Rodrigues, High efficiency photocatalytic water splitting using 2D α-Fe_2O_3/g-C_3N_4 Z-scheme catalysts, Adv. Energy Mater. 7 (2017) 1700025.
[5] I. Chakraborty, Z. Guo, B. Anirban, P. Sahoo, Physical modifications and algorithmic predictions behind further advancing 2D water splitting photocatalyst: an overview, Eng. Sci. 20 (2022) 34–46.
[6] C. Bie, L. Wang, J. Yu, Challenges for photocatalytic overall water splitting, Chem. (2022).
[7] Y. Jiang, Z. Sun, Q. Chen, C. Cao, Y. Zhao, W. Yang, L. Zeng, L. Huang, Fabrication of 0D/2D TiO_2 nanodots/g-C_3N_4 S-scheme heterojunction photocatalyst for efficient photocatalytic overall water splitting, Appl. Surf. Sci. 571 (2022) 151287.
[8] H. Zhao, H. Fu, X. Yang, S. Xiong, D. Han, X. An, MoS_2/CdS rod-like nanocomposites as high-performance visible light photocatalyst for water splitting photocatalytic hydrogen production, Int. J. Hydrogen. Energy 47 (2022) 8247–8260.
[9] W. Li, J. Li, X. Wang, Q. Chen, Preparation and water-splitting photocatalytic behavior of S-doped WO_3, Appl. Surf. Sci. 263 (2012) 157–162.
[10] S.-H. Chen, Y.-S. Jiang, H.-y. Lin, Easy synthesis of $BiVO_4$ for photocatalytic overall water splitting, ACS. Omega 5 (2020) 8927–8933.
[11] H. Gao, D. Zhang, M. Yang, S. Dong, Photocatalytic behavior of fluorinated rutile TiO_2 (110) surface: understanding from the band model, Sol. RRL. 1 (2017) 1700183.
[12] P. Zhou, J. Yu, M. Jaroniec, All-solid-state Z-scheme photocatalytic systems, Adv. Materials 26 (2014) 4920–4935.
[13] Y. Wang, J. Yu, W. Xiao, Q. Li, Microwave-assisted hydrothermal synthesis of graphene based Au–TiO $_2$ photocatalysts for efficient visible-light hydrogen production, J. Mater. Chem. A 2 (2014) 3847–3855.
[14] M. Das, S. Roy, Polypyrrole and associated hybrid nanocomposites as chemiresistive gas sensors: a comprehensive review, Mater. Sci. Semicond. Process. 121 (2021) 105332.
[15] N. Nie, L. Zhang, J. Fu, B. Cheng, J. Yu, Self-assembled hierarchical direct Z-scheme g-C_3N_4/ZnO microspheres with enhanced photocatalytic CO_2 reduction performance, Appl. Surf. Sci. 441 (2018) 12–22.
[16] A. Hayat, J.A.S. Syed, A.G. Al-Sehemi, K.S. El-Nasser, T. Taha, A.A. Al-Ghamdi, M. A. Amin, Z. Ajmal, W. Iqbal, A. Palamanit, State of the art advancement in rational design of g-C_3N_4 photocatalyst for efficient solar fuel transformation, environmental decontamination and future perspectives, Int. J. Hydrogen. Energy (2022).
[17] C. Zhang, D. Qin, Y. Zhou, F. Qin, H. Wang, W. Wang, Y. Yang, G. Zeng, Dual optimization approach to Mo single atom dispersed g-C_3N_4 photocatalyst: morphology and defect evolution, Appl. Catal. B Environ. 303 (2022) 120904.
[18] A. Hayat, M. Sohail, J.Ali Shah Syed, A.G. Al-Sehemi, M.H. Mohammed, A.A. Al-Ghamdi, T. Taha, H. Salem AlSalem, A.M. Alenad, M.A. Amin, Recent advancement of the current aspects of g-C_3N_4 for its photocatalytic applications in sustainable energy system, Chem. Record 22 (2022) e202100310.
[19] D. Wang, J. Chen, X. Gao, Y. Ao, P. Wang, Maximizing the utilization of photo-generated electrons and holes of g-C_3N_4 photocatalyst for harmful algae inactivation, Chem. Eng. J. 431 (2022) 134105.
[20] S. Ganguly, P. Das, M. Bose, T.K. Das, S. Mondal, A.K. Das, N.C. Das, Sonochemical green reduction to prepare Ag nanoparticles decorated graphene sheets for catalytic performance and antibacterial application, Ultrason. Sonochem. 39 (2017) 577–588.
[21] M. Das, D.P. Ura, P.K. Szewczyk, K. Berniak, U. Stachewicz, Thermal energy storage efficacy and buffering effect of liquid polyethylene glycol in core-shell polycarbonate and reduced graphene oxide fibers, Available at SSRN 4646107.
[22] F. Chen, H. Yang, X. Wang, H. Yu, Facile synthesis and enhanced photocatalytic H_2-evolution performance of NiS2-modified g-C_3N_4 photocatalysts, Chin. J. Catal. 38 (2017) 296–304.
[23] P. Zhang, T. Wang, H. Zeng, Design of Cu-Cu_2O/g-C_3N_4 nanocomponent photocatalysts for hydrogen evolution under visible light irradiation using water-soluble erythrosin B dye sensitization, Appl. Surf. Sci. 391 (2017) 404–414.
[24] J. Xu, J. Song, Y. Min, Q. Xu, P. Shi, Mg-induced g-C_3N_4 synthesis of nitrogen-doped graphitic carbon for effective activation of peroxymonosulfate to degrade organic contaminants, Chin. Chem. Lett. 33 (2022) 3113–3118.
[25] S. Zhang, H. Lan, Y. Cui, X. An, H. Liu, J. Qu, Insight into the key role of Cr intermediates in the efficient and simultaneous degradation of organic contaminants and Cr (VI) reduction via g-C_3N_4-assisted photocatalysis, Environ. Sci. Technol. 56 (2022) 3552–3563.

[26] Q. Wang, Z. Fang, W. Zhang, D. Zhang, High-efficiency g-C_3N_4 based photocatalysts for CO_2 reduction: modification methods, Adv. Fiber. Mater. 4 (2022) 342–360.

[27] Q. Xu, Z. Xia, J. Zhang, Z. Wei, Q. Guo, H. Jin, H. Tang, S. Li, X. Pan, Z. Su, Recent advances in solar-driven CO_2 reduction over g-C_3N_4-based photocatalysts, Carbon Energy 5 (2023) e205.

[28] A. Mehtab, S.M. Alshehri, T. Ahmad, Photocatalytic and photoelectrocatalytic water splitting by porous g-C_3N_4 nanosheets for hydrogen generation, ACS. Appl. Nano Mater. 5 (2022) 12656–12665.

[29] D.S. Pattanayak, D. Pal, J. Mishra, C. Thakur, K.L. Wasewar, Doped graphitic carbon nitride (g-C3N4) catalysts for efficient photodegradation of tetracycline antibiotics in aquatic environments, Environ. Sci. Pollut. Res. (2022) 1–8.

[30] Y. Cao, S. Alsharif, A. El-Shafay, Preparation, suppressed the charge carriers recombination, and improved photocatalytic performance of g-C_3N_4/MoS_2 pn heterojunction photocatalyst for tetracycline and dyes degradation upon visible light, Mater. Sci. Semicond. Process. 144 (2022) 106569.

[31] Y. Li, J. Zhong, J. Li, Reinforced photocatalytic H_2 generation behavior of S-scheme NiO/g-C_3N_4 heterojunction photocatalysts with enriched nitrogen vacancies, Opt Mater 135 (2023) 113296.

[32] P. John, K. Johari, N. Gnanasundaram, A. Appusamy, M. Thanabalan, Enhanced photocatalytic performance of visible light driven TiO_2/g-C_3N_4 for degradation of diclofenac in aqueous solution, Environ. Technol. Innov. 22 (2021) 101412.

[33] L. Biswal, S. Nayak, K. Parida, Recent progress on strategies for the preparation of 2D/2D MXene/gC $_3$ N $_4$ nanocomposites for photocatalytic energy and environmental applications, Catal. Sci. Technol. 11 (2021) 1222–1248.

[34] P. Das, S. Ganguly, S. Banerjee, N.C. Das, Graphene based emergent nanolights: a short review on the synthesis, properties and application, Res. Chem. Intermediates 45 (2019) 3823–3853.

[35] S. Ganguly, N. Kanovsky, P. Das, A. Gedanken, S. Margel, Photopolymerized thin coating of polypyrrole/graphene nanofiber/iron oxide onto nonpolar plastic for flexible electromagnetic radiation shielding, strain sensing, and non-contact heating applications, Adv. Mater. Interfaces. 8 (2021) 2101255.

[36] M. Mishra, D.-M. Chun, α-Fe_2O_3 as a photocatalytic material: a review, Appl. Catal. A Gener. 498 (2015) 126–141.

[37] J. Wang, C. Qin, H. Wang, M. Chu, A. Zada, X. Zhang, J. Li, F. Raziq, Y. Qu, L. Jing, Exceptional photocatalytic activities for CO2 conversion on AlO bridged g-C_3N_4/α-Fe_2O_3 z-scheme nanocomposites and mechanism insight with isotopesZ, Appl. Catal. B Environ. 221 (2018) 459–466.

[38] J.N. Coleman, M. Lotya, A. O'Neill, S.D. Bergin, P.J. King, U. Khan, K. Young, A. Gaucher, S. De, R.J. Smith, Two-dimensional nanosheets produced by liquid exfoliation of layered materials, Science 331 (2011) 568–571.

[39] Q. Liu, Y. Guo, Z. Chen, Z. Zhang, X. Fang, Constructing a novel ternary Fe (III)/graphene/g-C_3N_4 composite photocatalyst with enhanced visible-light driven photocatalytic activity via interfacial charge transfer effect, Appl. Catal. B Environ. 183 (2016) 231–241.

[40] C. Kim, K.M. Cho, K. Park, K.H. Kim, I. Gereige, H.T. Jung, Ternary hybrid aerogels of g-C_3N_4/α-Fe_2O_3 on a 3D graphene network: an efficient and recyclable Z-scheme photocatalyst, Chempluschem. 85 (2020) 169–175.

[41] M. Danish, M.S. Athar, I. Ahmad, M.Z. Warshagha, Z. Rasool, M. Muneer, Highly efficient and stable Fe_2O_3/g-C_3N_4/GO nanocomposite with Z-scheme electron transfer pathway: role of photocatalytic activity and adsorption isotherm of organic pollutants in wastewater, Appl. Surf. Sci. 604 (2022) 154604.

[42] Y. Wu, J. Ward-Bond, D. Li, S. Zhang, J. Shi, Z. Jiang, g-C_3N_4@ α-Fe_2O_3/C photocatalysts: synergistically intensified charge generation and charge transfer for NADH regeneration, ACS. Catal. 8 (2018) 5664–5674.

[43] N. Farooq, A. ur Rehman, A.M. Qureshi, Z. ur Rehman, A. Ahmad, M.K. Aslam, H. M.A. Javed, S. Hussain, M.A. Habila, N. AlMasoud, Au@ GO@ g-C_3N_4 and Fe_2O_3 nanocomposite for efficient photocatalytic and electrochemical applications, Surf. Interfaces. 26 (2021) 101399.

[44] L.T. Hang, N.D. Lai, N.T. Phuong, D.V. Thang, N.M. Hung, N. Van Minh, Influence of annealing temperature on physical properties and photocatalytic ability of g-C_3N_4 nanosheets synthesized through urea polymerization in Ar atmosphere, Phys. B Condens. Matter 532 (2018) 48–53.

[45] M. Karmaoui, L. Lajaunie, D.M. Tobaldi, G. Leonardi, C. Benbayer, R. Arenal, J. A. Labrincha, G. Neri, Modification of anatase using noble-metals (Au, Pt, Ag): toward a nanoheterojunction exhibiting simultaneously photocatalytic activity and plasmonic gas sensing, Appl. Catal. B Environ. 218 (2017) 370–384.

[46] P. Kubelka, F. Munk, An article on optics of paint layers, Z. Tech. Phys 12 (1931) 259–274.

[47] S. Komornicki, M. Radecka, P. Sobaś, Structural, electrical and optical properties of TiO_2–WO_3 polycrystalline ceramics, Mater. Res. Bull. 39 (2004) 2007–2017.

[48] J.I. Pankove, Optical processes on semiconductors Dover publication, Inc. New york (1971).

[49] W. Touati, M. Karmaoui, A. Bekka, M.F. Edelmannová, C. Furgeaud, A. Chakib, I. kadi Allah, B. Figueiredo, J. Labrincha, R. Arenal, Photocatalytic hydrogen generation from a methanol–water mixture in the presence of gC $_3$ N $_4$ and graphene/gC $_3$ N$_4$, New J. Chem. 46 (2022) 20679–20690.

[50] Z. Sun, G. Yao, X. Zhang, S. Zheng, R.L. Frost, Enhanced visible-light photocatalytic activity of kaolinite/g-C_3N_4 composite synthesized via mechanochemical treatment, Appl. Clay. Sci. 129 (2016) 7–14.

[51] S. Matsumoto, E.-Q. Xie, F. Izumi, On the validity of the formation of crystalline carbon nitrides, C3N4, Diam. Relat. Mater. 8 (1999) 1175–1182.

[52] Q. Han, D. Zhang, J. Guo, B. Zhu, W. Huang, S. Zhang, Improved catalytic performance of Au/α-Fe_2O_3-like-worm catalyst for low temperature CO oxidation, Nanomaterials 9 (2019) 1118.

[53] S. Wang, D. Lou, Z. Wang, N. Yu, H. Wang, Z. Chen, L. Zhang, Synthesis of ultrathin g-C_3N_4/graphene nanocomposites with excellent visible-light photocatalytic performances, Function. Mater. Lett. 12 (2019) 1950025.

[54] L. Lajaunie, C. Pardanaud, C. Martin, P. Puech, C. Hu, M. Biggs, R. Arenal, Advanced spectroscopic analyses on a: CH materials: revisiting the EELS characterization and its coupling with multi-wavelength raman spectroscopy, Carbon. N. Y. 112 (2017) 149–161.

[55] E. Oswald, A.L. Gaus, J. Kund, M. Küllmer, J. Romer, S. Weizenegger, T. Ullrich, A. K. Mengele, L. Petermann, R. Leiter, Cobaloxime complex salts: synthesis, patterning on carbon nanomembranes and heterogeneous hydrogen evolution studies, Chem. Eur. J. 27 (2021) 16896–16903.

[56] F. Dong, Y. Li, Z. Wang, W.-K. Ho, Enhanced visible light photocatalytic activity and oxidation ability of porous graphene-like g-C_3N_4 nanosheets via thermal exfoliation, Appl. Surf. Sci. 358 (2015) 393–403.

[57] D.M. Sherman, T.D. Waite, Electronic spectra of Fe^{3+} oxides and oxide hydroxides in the near IR to near UV, Am. Mineralogist 70 (1985) 1262–1269.

[58] D. Tobaldi, D. Dvoranová, L. Lajaunie, N. Rozman, B. Figueiredo, M. Seabra, A. S. Škapin, J. Calvino, V. Brezová, J. Labrincha, Graphene-TiO_2 hybrids for photocatalytic aided removal of VOCs and nitrogen oxides from outdoor environment, Chem. Eng. J. 405 (2021) 126651.

[59] Q. Xu, B. Zhu, C. Jiang, B. Cheng, J. Yu, Constructing 2D/2D Fe_2O_3/g-C_3N_4 direct Z-scheme photocatalysts with enhanced H_2 generation performance, Sol. RRL. 2 (2018) 1800006.

[60] H. Shen, X. Zhao, L. Duan, R. Liu, H. Li, Enhanced visible light photocatalytic activity in SnO_2@ g-C_3N_4 core-shell structures, Mater. Sci. Eng. B 218 (2017) 23–30.

[61] S. Babar, N. Gavade, H. Shinde, A. Gore, P. Mahajan, K.H. Lee, V. Bhuse, K. Garadkar, An innovative transformation of waste toner powder into magnetic g-C_3N_4-Fe_2O_3 photocatalyst: sustainable e-waste management, J. Environ. Chem. Eng. 7 (2019) 103041.

[62] P. Mallick, B. Dash, X-ray diffraction and UV-visible characterizations of α-Fe_2O_3 nanoparticles annealed at different temperature, Nanosci. Nanotechnol 3 (2013) 130–134.

[63] A.M. Pennington, A.I. Okonmah, D.T. Munoz, G. Tsilomelekis, F.E. Celik, Changes in polymorph composition in P25-TiO_2 during pretreatment analyzed by differential diffuse reflectance spectral analysis, J. Phys. Chem. C 122 (2018) 5093–5104.

[64] D. Zeng, T. Zhou, W.-J. Ong, M. Wu, X. Duan, W. Xu, Y. Chen, Y.-A. Zhu, D.-L. Peng, Sub-5 nm ultra-fine FeP nanodots as efficient co-catalysts modified porous g-C3N4 for precious-metal-free photocatalytic hydrogen evolution under visible light, ACS. Appl. Mater. Interfaces. 11 (2019) 5651–5660.

[65] H.G. Cha, J. Song, H.S. Kim, W. Shin, K.B. Yoon, Y.S. Kang, Facile preparation of Fe_2 O_3 thin film with photoelectrochemical properties, Chem. Commun. 47 (2011) 2441–2443.

[66] D. Tobaldi, K. Kočí, M. Edelmannová, L. Lajaunie, B. Figueiredo, J. Calvino, M. Seabra, J. Labrincha, CuxO and carbon–modified TiO_2–based hybrid materials for photocatalytically assisted H_2 generation, Mater. Today Energy 19 (2021) 100607.

[67] M. Luo, J. Xu, W. Xu, Y. Zheng, G. Wu, T. Jeong, Photocatalytic activity of MoS_2 nanoflower-modified CaTiO3 composites for degradation of RhB under visible light, Nanomaterials 13 (2023) 636.

[68] H. Dong, J. Sun, G. Chen, C. Li, Y. Hu, C. Lv, An advanced Ag-based photocatalyst Ag $_2$ Ta$_4$ O $_{11}$ with outstanding activity, durability and universality for removing organic dyes, Phys. Chem. Chem. Phys. 16 (2014) 23915–23921.

[69] S. Hmamouchi, A. El Yacoubi, B.C. El Idrissi, Using egg ovalbumin to synthesize pure α-Fe_2O_3 and cobalt doped α-Fe_2O_3: structural, morphological, optical and photocatalytic properties, Heliyon. 8 (2022) e08953.

[70] S.-J. Liang, L. Ang, Electron thermionic emission from graphene and a thermionic energy converter, Phys. Rev. Appl. 3 (2015) 014002.

[71] Y. Hong, Y. Jiang, C. Li, W. Fan, X. Yan, M. Yan, W. Shi, In-situ synthesis of direct solid-state Z-scheme V_2O_5/g-C_3N_4 heterojunctions with enhanced visible light efficiency in photocatalytic degradation of pollutants, Appl. Catal. B Environ. 180 (2016) 663–673.

[72] S. Chahal, A. Kumar, P. Kumar, Zn doped α-Fe_2O_3: an efficient material for UV driven photocatalysis and electrical conductivity, Crystals. (Basel) 10 (2020) 273.

[73] J. Zhang, F. Ren, M. Deng, Y. Wang, Enhanced visible-light photocatalytic activity of a gC$_3$ N $_4$/BiVO $_4$ nanocomposite: a first-principles study, Phys. Chem. Chem. Phys. 17 (2015) 10218–10226.

[74] N. Todorova, I. Papailias, T. Giannakopoulou, N. Ioannidis, N. Boukos, P. Dallas, M. Edelmannová, M. Reli, K. Kočí, C. Trapalis, Photocatalytic H_2 evolution, CO_2 reduction, and NOx oxidation by highly exfoliated g-C_3N_4, Catalysts. 10 (2020) 1147.

[75] R. Qian, H. Zong, J. Schneider, G. Zhou, T. Zhao, Y. Li, J. Yang, D.W. Bahnemann, J.H. Pan, Charge carrier trapping, recombination and transfer during TiO2 photocatalysis: an overview, Catal. Today 335 (2019) 78–90.

[76] Y. Kumar, R. Kumar, P. Raizada, A.A.P. Khan, A. Singh, Q. Van Le, V.-H. Nguyen, R. Selvasembian, S. Thakur, P. Singh, Current status of hematite (α-Fe_2O_3) based Z-scheme photocatalytic systems for environmental and energy applications, J. Environ. Chem. Eng. 10 (2022) 107427.

[77] T. Taniike, K. Takahashi, The value of negative results in data-driven catalysis research, Nat. Catal. 6 (2023) 108–111.